IOPscience iopscience.iop.org

Home Search Collections Journals About Contact us My IOPscience

Two-Dimensional Carrier Profiling by Kelvin-Probe Force Microscopy

This content has been downloaded from IOPscience. Please scroll down to see the full text.

2008 Jpn. J. Appl. Phys. 47 4448

(http://iopscience.iop.org/1347-4065/47/6R/4448)

View the table of contents for this issue, or go to the journal homepage for more

Download details:

IP Address: 140.113.38.11
This content was downloaded on 25/04/2014 at 16:06

Please note that terms and conditions apply.

Japanese Journal of Applied Physics
Vol. 47, No. 6, 2008, pp. 4448–4453

©2008 The Japan Society of Applied Physics

Two-Dimensional Carrier Profiling by Kelvin-Probe Force Microscopy

Bing-Yue TSUI*, Chih-Ming HSIEH, Po-Chih SU, Shien-Der TZENG[1], and Shangjr GWO[1]

Department of Electronics Engineering and Institute of Electronics, National Chiao Tung University, Hsinchu 300, Taiwan, R.O.C.
[1]*Department of Physics, National Tsing-Hua University, Hsinchu 300, Taiwan, R.O.C.*

(Received June 20, 2007; accepted February 17, 2008; published online June 13, 2008)

This paper reports the two-dimensional (2-D) carrier/dopant profiling technique by Kelvin-probe force microscopy (KFM). Before surface potential was measured, a feedback control circuit was used to improve signal response speed. The effect of surface treatment on the contrast in surface potential images was studied. Then the correlation between surface potential difference measured by KFM and surface carrier/dopant concentration obtained by spreading resistance profiling, the capacitance–voltage method, and secondary ion mass spectroscopy analysis was established. On the basis of these results, the carrier depth profiling of a p–n junction and the detection of a p–n junction array with small pitch have been successfully demonstrated. [DOI: 10.1143/JJAP.47.4448]

KEYWORDS: Kelvin-probe force microscopy, scanning probe microscopy, surface potential

1. Introduction

As semiconductor devices scale down to the nano-regime, the measurement of two-dimensional (2-D) carrier/dopant distribution becomes more and more important in order to simulate and model device performance precisely. However, the typical spreading resistance profiling (SRP) technique and secondary ion mass spectroscopy (SIMS) measure one-dimensional (1-D) depth profiles. Although some special SIMS techniques have been proposed to measure 2-D depth profiles, the spatial resolution is not sufficient.[1,2] Therefore, 2-D carrier/dopant distribution for traditional device modeling is estimated first from a 1-D depth profile done by SIMS analysis, and then technology computer aided design (TCAD) tools have been used to simulate device characteristics while adjusting the 2-D dopant distribution until the measured device characteristics are well fitted. Since the adjusted 2-D dopant distribution may be not the actual distribution, the error between the actual and the adjusted dopant distributions makes device modeling more and more difficult as devices scale down into the nano-regime.

Scanning probe microscopy (SPM) is one of the most powerful surface analysis techniques.[3,4] Scanning capacitance microscopy (SCM)[5–10] and Kelvin-probe force microscopy (KFM)[11–13] are the two major operating modes of SPM for 2-D carrier/dopant distribution measurement. They are non-destructive techniques with high spatial resolution. For SCM, the accuracy often depends on many undetermined parameters and complex calculations. A uniform and high quality dielectric on the sample surface is required for SCM; however, the dielectric formation process may change the dopant distribution. The derivative of dC/dV also generates noise during data manipulation.

The KFM is a surface potential measurement technique for conductive samples, and the theoretical principle behind it has been well derived.[11,14] However, the sample's surface potential is very sensitive to surface charges and to adsorb the molecules. The most common method in KFM is to use a high vacuum chamber, smaller conductive tips, and *in-situ* heating to reduce any external influence on surface potential.[15–17] The spatial resolution of KFM is influenced by the tip diameter as well as the signal response speed. The tip diameter could be reduced greatly by attaching a carbon nanotube (CNT) to the end of a conventional tip. The signal response time could be improved by adding an external feedback control circuit.

In this paper, the basic theory of KFM is briefly introduced. The system setup and the effect of a feedback control circuit on the signal response speed are described. Several surface treatment methods were studied to obtain stable and high contrast surface potential images. The correlation between surface potential difference of a p–n junction ($\Delta\phi_{pn}$) and carrier/dopant concentration has been established for the first time. Finally, the cross-sectional depth profiling of a p–n junction and the detection of p–n junction array have been successfully demonstrated.

2. Operating Principle and System Setup

KFM is known as a surface potential microscopy based on non-contacting mode AFM. The purpose of KFM is to measure the potential offset between a probe tip and sample surface.[18] Figure 1 shows a block diagram of the high vacuum KFM system (Seiko Instruments SPA300HV) used in this work. The vacuum in this system can be better than 1×10^{-6} Torr. The cantilever we used is a PtIr coated silicon tip with a typical tip radius of ~20 nm. The force constant and resonant requency of tip were about 1.5 N/m and 60 kHz, respectively. By using a dual-modulation scheme (with both mechanical and electrical modulations) at two non-interfering modulation frequencies, AFM topographic and KFM surface potential images can be obtained simulta-

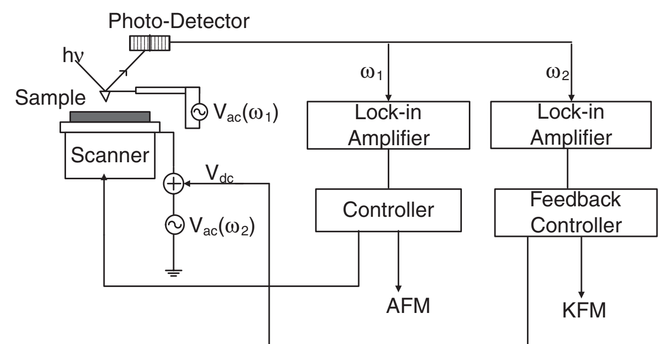

Fig. 1. Block diagram of the KFM with an external feedback control module used in this work.

*E-mail address: bytsui@mail.nctu.edu.tw

neously. The vibration frequency of the tip (ω_1) was chosen to be slightly lower than the resonant frequency of the tip (60 kHz) and the typical vibration amplitude was about 100 mV. We use the tapping mode for measurement, which reduces damage to the tips. The appropriate ac modulation voltage (V_{ac}) and frequency ($\omega_2 = 20-80$ kHz) were chosen based on the response between the sample and the tip. Although the Q-factor of a free-oscillating cantilever in a vacuum is usually high (~10,000), the KFM is operated in the tapping mode with a reduced Q-factor. Therefore, an additional feedback control circuit was inserted to improve the response speed.

Equation (1) expresses the total force experienced by the tip in a KFM system. The total force (F_t) is composed of the van der Waals force (F_a), capacitance force (F_c), and coulomb electrostatic force (F_e).[9,11,12,16)]

$$
\begin{aligned}
F_t &= F_a + F_c + F_e \\
&= F_a + \frac{1}{2}\frac{\partial C}{\partial z}V^2 - \frac{q_{tip}q_e}{4\pi\varepsilon z^2} \\
&= F_a + \frac{1}{2}\frac{\partial C}{\partial z}(V_{dc}-V_s)^2 + \frac{\partial C}{\partial z}\frac{{V_{ac}}^2}{4} \\
&\quad + \frac{{q_e}^2}{4\pi\varepsilon z^2} + \frac{q_e C(V_{dc}-V_s)}{4\pi\varepsilon z^2} \\
&\quad + \left[\frac{\partial C}{\partial z}(V_{dc}-V_s) + \frac{q_e C}{4\pi\varepsilon z^2}\right]\cdot V_{ac}\sin\omega_2 t \\
&\quad - \frac{\partial C}{\partial z}\frac{{V_{ac}}^2}{4}\cos(2\omega_2 t),
\end{aligned}
\tag{1}
$$

where C is the tip–sample capacitance, which is a function of their separation distance z, q_{tip} is the total charge on the tip, q_e is the charge on sample surface, ε is the effective permittivity between the tip charge and surface charge, V_{dc} is the dc potential difference between tip and sample, V_{ac} is the amplitude of the ac modulation signal with frequency ω_2, and $2\omega_2$ is the second harmonic frequency. A lock-in amplifier is used to lock the signal ω_2 and determine its amplitude. If the surface charge (q_e) is zero, we can calculate $V_{dc} - V_s$. Finally, we can determine $V_{dc} = V_s =$ surface potential using the crossing feedback control circuit.

A map of the nulling dc potential versus the lateral position coordinate produces an image of the work function of the surface. The work function relates to many surface phenomena, including catalytic activity, reconstruction of surfaces, doping and band-bending of semiconductors, charge trapping in dielectrics, and corrosion. The map of the work function produced by KFM gives information about the composition and electronic state of the local structures on the surface of a solid.

Figure 2 illustrates a p–n junction that is measured by KFM. Theoretically, the measured results of p- and n-type regions by KFM should be the work function difference between the tip and the Si surface. As shown in Fig. 2(b), we can obtain the surface potential ($\phi_m - \phi_n$) on n-type region and ($\phi_m - \phi_p$) on a p-type region, where ϕ_m is the work function of tip, ϕ_n is the work function of the n-type region, and ϕ_p is the work function of the p-type region. Their potential difference, $\phi_p - \phi_n$, is the same as the built-in voltage ϕ_b if there is no surface charge on the sample.[10)]

The feedback control circuit dominates the spatial resolution of the potential image because the response of the feedback circuit must be faster than the speed of data sampling. In order to have more data points, i.e., better resolution, over the same scanning area, the feedback circuit must respond faster. Using a built-in circuit, a scanning tail is clearly observed, and the shape of the junction is different when scanned in different directions, as shown in Fig. 3. Due to the signal delay, a large horizontal shift between the two surface potential profiles scanned in different directions is observed. To solve this problem, a new feedback control circuit was implemented to replace the built-in circuit, as shown in Fig. 4. Figure 5 shows the surface potential of a planar p–n junction detected by KFM with a built-in feedback control circuit. As we see, the potential image and scanning response are improved.

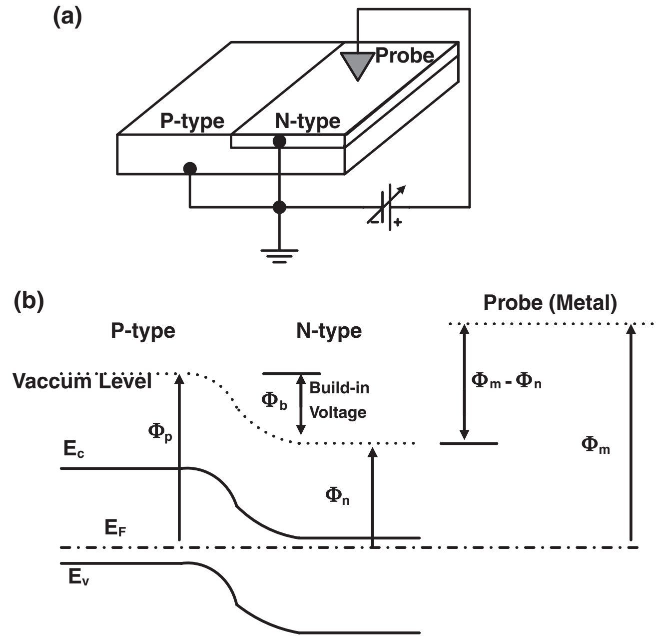

Fig. 2. (a) Circuit and (b) Ban diagram schematic drawing of a p–n junction measured by a KFM system.[14)]

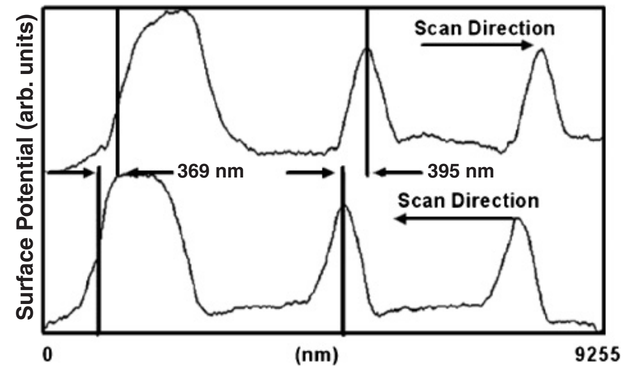

Fig. 3. Surface potential image of a p–n junction measured by KFM with a built-in feedback control circuit.

3. Experimental Procedure

The starting material was a (100)-oriented 4-in.-diameter Si wafer. The n-type wafers were phosphorous-doped and the p-type wafers were boron-doped. The doping concentration determined by the SRP technique is 5×10^{14} cm^{-3} for a p-type wafer and 2×10^{15} cm^{-3} for an n-type wafer.

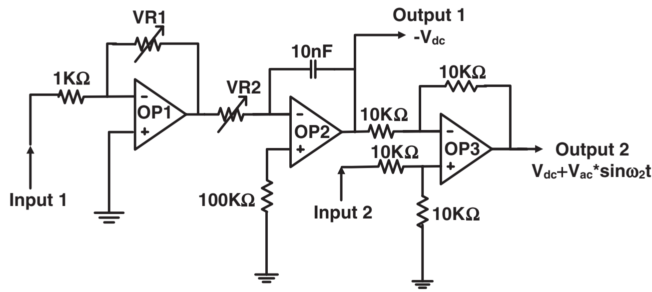

Fig. 4. Block diagram of the external feedback control circuit.

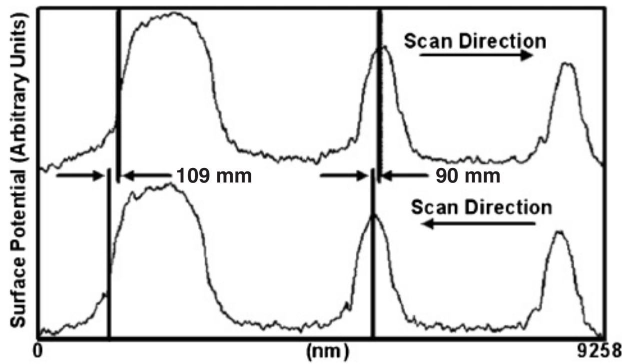

Fig. 5. Surface potential image of a p–n junction measured by KFM with an external feedback control circuit.

Two sets of samples were prepared. In the first sample set, periodic n^+–p and p^+–n junctions with different doping concentrations were fabricated in order to establish a correlation between surface potential difference and carrier/dopant concentration difference. After the typical RCA cleaning, the n^+ and p^+ regions were defined by lithography. As^+ ions and $BF_2{}^+$ ions were implanted to form n^+ and p^+ junctions, respectively, at a dose level of 1×10^{13}, 5×10^{13}, 1×10^{14}, 2×10^{14}, 1×10^{15}, 2×10^{15}, and 5×10^{15} cm^{-2}. The implantation energies for As^+ and $BF_2{}^+$ were both 20 keV. After ion implantation, a 200-nm-thick SiO_2 film was deposited on the wafer surface in a plasma enhanced chemical vapor deposition (PECVD) system to prevent the dopant from diffusing out during the thermal activation at 950 °C for 30 min. The capping SiO_2 layer was removed by dilute HF (DHF) solution, and different surface treatments were performed on the samples with As^+ ion implantation at a dose of 5×10^{15} cm^{-2} before KFM measurement to determine the most suitable surface preparation method. Table I summarizes the sample ID and the surface treatment methods.

The second sample set has the n^+–n and p^+–p high-low junction structure. These samples were used to determine the surface concentration by conventional methods. The n^+ and p^+ doping conditions are identical to those used for the first sample set. The surface concentrations of samples with lower implantation doses were determined by the capacitance–voltage (C–V) method[19–21] and SIMS[22] while the surface concentrations of samples with higher implantation doses were determined by SRP.[23,24]

For C–V measurement, a 48-nm-thick SiO_2 layer was deposited on the sample surface in a PECVD system at 350 °C. An Al gate electrode was deposited in a thermal evaporation system and patterned by lithography and wet etching. The process temperatures were low enough so that dopant redistribution can be ignored. Because of the limitation of the Debye length (L_D), the concentration at the first $3L_D$ is not valid.[20] For highly concentrated samples, the L_D should be replaced by the Thomas–Fermi length (L_{TF}) due to quantum effects, and then the resultant concentration becomes more plausible.[20] The SRP measurements were performed at two different laboratories: the Nano Facility Center of the National Chiao-Tung University and Episil Technology. Both sites used the SSM 150 spreading resistance system. The systems were calibrated with standard Si calibration kits before measurement. The SIMS analyses were performed at three different sites using Cameca IMS-5F, Cameca IMS-4F, and Cameca IMS-5F facilities. The primary ions were Cs^+ for As depth profiling and $O_2{}^+$ for B depth profiling. The SIMS counts over the first 10 nm are unstable so that the concentrations 20 nm deep were treated as the surface concentration. Furthermore, SIMS detects dopants but not carriers so that the measured dopant concentration is higher than the actual carrier concentration.

Table I. Surface treatment methods and samples IDs used in this work.

Surface treatment	Sample ID			
	A	B	C	D
ACE immersion 3–5 min	V	V	V	V
100 : 1 HF dipped ~20 s	V	V		
Rapid thermal oxidation 900 °C, 1 min			V	
$H_2SO_4 : H_2O_2 = 3:1$, 100 °C, 10 min				V
DI water rinse	V		V	V

Since it is the carrier concentration which determines the surface potential, we adopt the C–V and the SIMS data for the three lower-implantation-dose samples and the SRP data for the three higher-implantation-dose samples. Therefore, we use “carrier” instead of “dopant” in the following sections.

4. Results and Discussion

4.1 *Effect of Surface treatment*

Figures 6(a)–6(d) show the measured surface potential images of samples A to D, respectively. The KFM measurement parameters are: $\omega_2 = 34$–38 kHz, $V_{ac} = 1.1$–1.5 V, and scanning speed ~ 0.05 Hz. It is clear that sample A shows the best potential image contrast and sample B shows the worst contrast. An X-ray photoelectron spectrometer (XPS) was used to analyze the surface condition of samples after different surface treatments. Figure 7 shows the F 1s binding energy of samples A and B. The peaks at 686 and 689.9 eV observed for sample B are the binding energy of Si–F and H–F, respectively. No F 1s signal was observed for sample A. Figure 8 shows the O 1s binding energies of samples A and B. The strong O–H peak in sample A suggests that Si–OH bonds substitute for the Si–F bonds after rinsing with deionized water (DI) water.[25,26] The reaction can be expressed as $Si–F + H_2O \rightarrow Si–OH + HF$. Sample B also exhibits an O–H bond, but the intensity is much weaker than that of sample A. Only Si–O bonds were detected on samples C and D, so that the data is not shown.

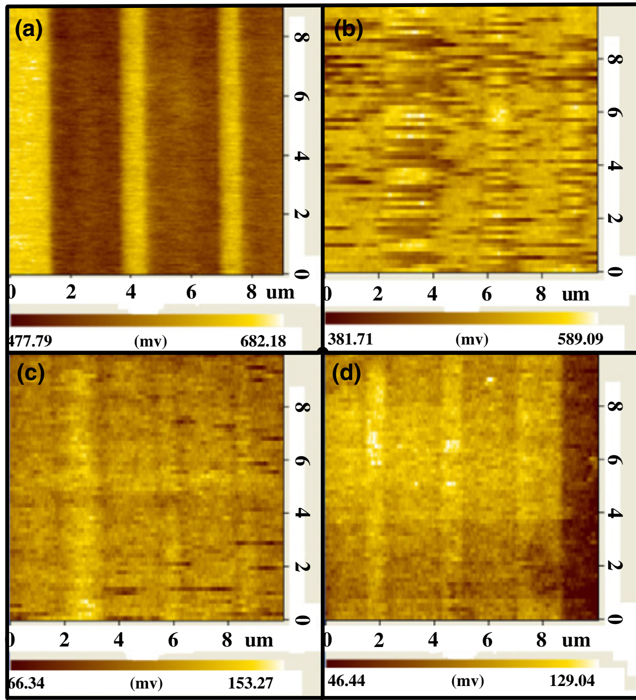

Fig. 6. (Color online) Surface potential images of samples A, B, C, and D measured by KFM. The surface treatment methods for the four samples are listed in Table I.

According to XPS analyses, it is clear that as the sample surface becomes covered by Si–O or Si–F bonds, the contrast in the surface potential image is degraded,[25,27] because the Si–F bond increases the surface charge (q_e) and has a larger dipole moment. The Si–O bond isolates the Si surface and increases the capacitance (C) between surface and tip. As shown in eq. (1), q_e and C are included in the amplitude of the ω_2 signal. With non-zero q_e and large C value, the term $V_{dc} - V_s$ cannot be determined directly from the amplitude of ω_2.

Therefore, the surface treatment procedure before KFM measurement is determined to be dipping in DHF followed by rinsing with DI water. To remove possible organic contamination, a 10-min ultrasonic oscillation in acetone may be performed before DHF dipping.

4.2 *Correlation between surface potential difference and surface carrier/dopant concentration*

Theoretically, the measured surface potential difference between the p- and n-regions of a p–n junction should be equal to the build-in voltage (ϕ_b), which is the Fermi-energy difference between n- and p-type Si. However, even if sample A shows the strongest image contrast, the measured surface potential difference ($\Delta\phi_{pn}$) between the n^+ region and the p-substrate is only 0.23 eV, which is much lower than the theoretical build-in voltage of about 0.8 eV. This discrepancy arises from the states existing on the sample surface. Equation (2) defines the situation:

$$\begin{aligned}\Delta\phi_{pn} &= (\phi_p - \Delta\phi_p) - (\phi_n - \Delta\phi_n)\\ &= (\phi_p - \phi_n) - (\Delta\phi_p - \Delta\phi_n) < (\phi_p - \phi_n) = \phi_b,\end{aligned} \tag{2}$$

where ϕ_p is the Fermi-level of the p-type Si region, ϕ_n is the Fermi-level of the n-type Si region, $\Delta\phi_p$ is the shift in the Fermi-level due to the surface states on the p-type Si region,

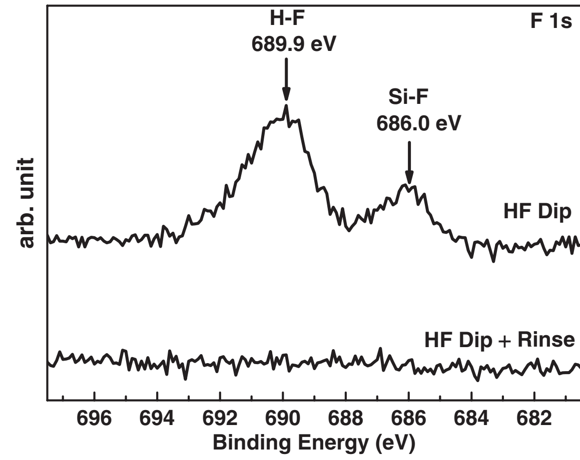

Fig. 7. The F 1s binding energies of samples A and B measured by XPS.

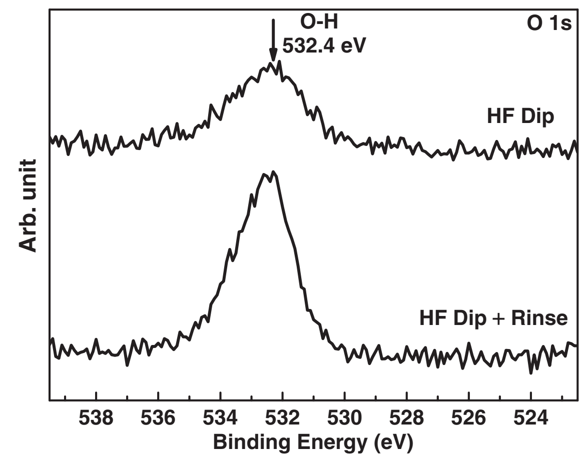

Fig. 8. The O 1s binding energies of samples A and B measured by XPS.

and $\Delta\phi_p$ is the shift in the Fermi-level due to the surface states on n-type Si. The surface states should trap surface charge to maintain charge neutrality. Usually, the trapped charge is positive on a p-type silicon surface and therefore reduces the surface charge concentration and the Fermi level. The $\Delta\phi_p$ may be derived as[28)]

$$\begin{aligned}C_p &= N_v \exp\left(\frac{E_i - q\phi_p}{kT}\right) \propto \exp\left(-\frac{q\phi_p}{kT}\right),\\ \frac{dC_p}{d\phi_p} &\propto -\exp\left(-\frac{q\phi_p}{kT}\right),\\ \Delta\phi_p &\propto -\Delta C_p \exp\left(\frac{q\phi_p}{kT}\right),\end{aligned} \tag{3}$$

where C_p is the hole concentration in the p-type Si, N_v is the energy state density of the valence band, and E_i is the intrinsic Fermi energy. As the n-type Si concentration (C_n) is fixed, $\Delta\phi_{pn}$ should be a function of e^{ϕ_b}; that is, ϕ_b is a function of $\ln(\Delta\phi_{pn})$. On the other hand,

$$\phi_b = kT \ln\left(\frac{C_p C_n}{{n_i}^2}\right), \tag{4}$$

where C_p and C_n are the majority carrier densities of the p- and n-type Si, respectively, and n_i is the intrinsic carrier density. In the case of fixed C_n, ϕ_b would be proportional to

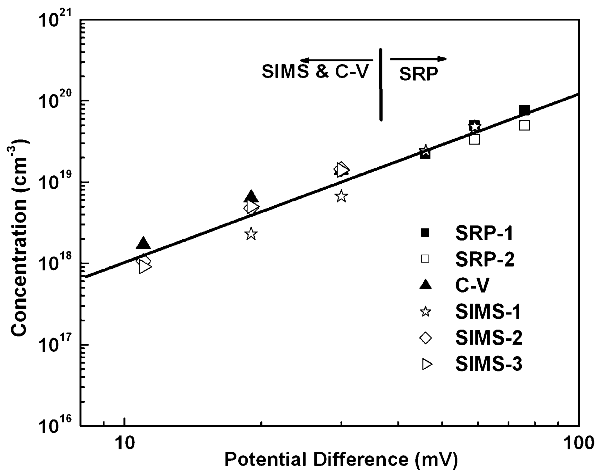

Fig. 9. Correlation between surface potential difference and surface carrier concentration of the n^+–p junctions with different As^+ ion implantation doses.

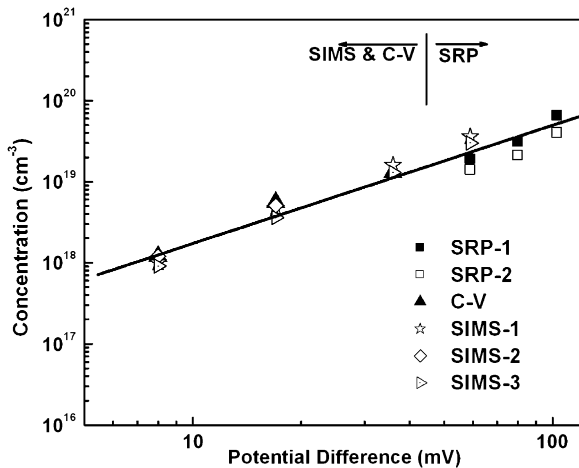

Fig. 10. Correlation between surface potential difference and surface carrier concentration of the p^+–n junctions with different BF_2^+ ion implantation doses.

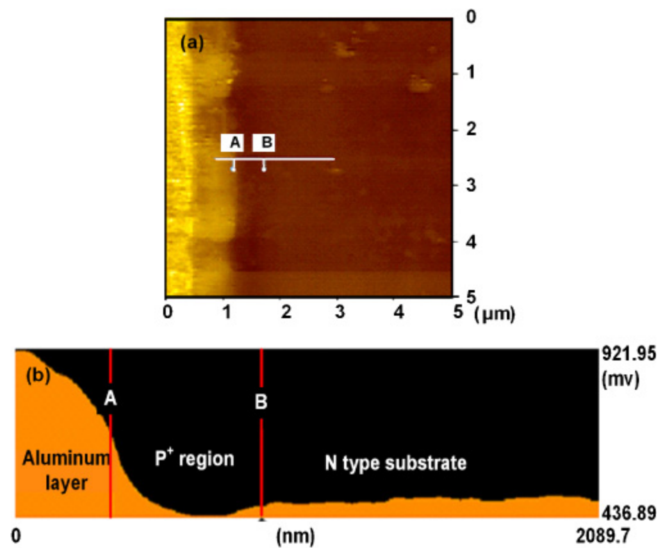

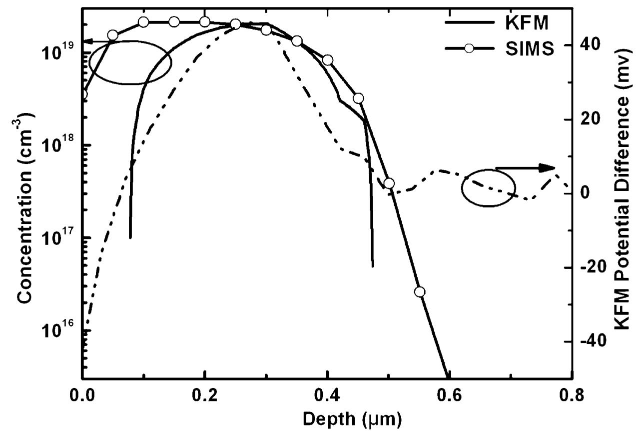

Fig. 11. (Color online) Surface image and the potential profile of a p^+–n junction in vertical direction after cleaving and polishing.

Fig. 12. Carrier depth profiles of the p^+–n junction shown in Fig. 11 measured by KFM and SIMS.

$\ln C_p$. Therefore, we conclude that $\ln(\Delta\phi_{pn})$ should be correlated with $\ln C_p$.

Several methods including the *C–V* method, SRP, and SIMS were employed to determine the surface carrier concentration in order to setup an experimental correlation between $\Delta\phi_{pn}$ and C_s. Figures 9 and 10 show the correlation between C_s and $\Delta\phi_{pn}$. A very good linear relationship is observed in the full-log plot. It is postulated that the carrier concentration is an exponential function of the Fermi energy, while the Fermi energy of a free Si surface depends on the surface charge. The shift of Fermi energy due to surface charge is an exponential function of the carrier concentration so that the measured surface potential difference is proportional to the surface concentration in the full-log plot. This result confirms the theoretical prediction. From Figs. 9 and 10, the empirical correlation between C_s and $\Delta\phi_{pn}$ can be established by

$$\log C_n = 15.938 + 2.073\log(\Delta\phi_{pn}) \quad \text{for } n^+\text{–p junction}, \quad (5)$$

$$\log C_p = 16.778 + 1.459\log(\Delta\phi_{pn}) \quad \text{for } p^+\text{–n junction}. \quad (6)$$

4.3 Depth profiling of p–n junction and detection of junction array

On the basis of eqs. (5) and (6), we can determine the depth profile of a p–n junction by measuring the surface potential. Figures 11(a) and 11(b) shows the surface potential image and the surface potential profile in the A–B direction of an Al-contacted p^+–n junction in the vertical direction after cleaving and polishing. The 500-nm-thick Al layer was deposited to help to determine the position of the p^+ surface. Point A is the interface between the Al and p^+ layer and was defined as the starting point of the junction surface.

Figure 12 shows the depth profiles measured by KFM and SIMS. The peak concentration and junction depth measured by KFM are consistent with those measured by SIMS. At the p^+ surface, the carrier concentration determined by KFM is much lower than the dopant concentration measured by SIMS. We postulate that it was affected by either the aluminum reference capping layer or the polishing defects at the Al/Si interface; the defect charges make the KFM measurement unstable in near surface region. The additional work is required to solve this in the future.

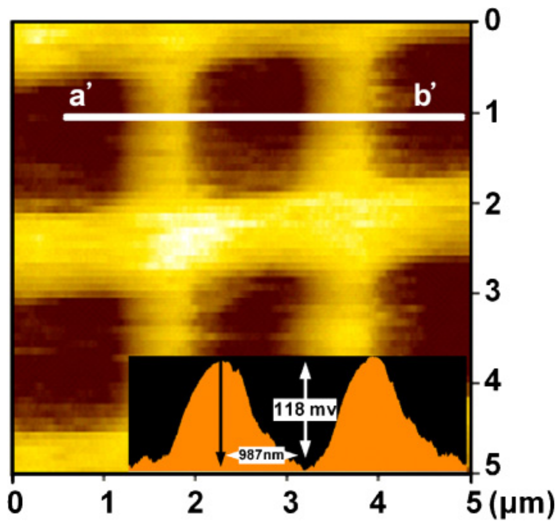

Fig. 13. (Color online) Surface potential image of a p–n junction array measured by KFM.

Figure 13 shows the surface image of a p–n junction array with a pitch of 0.8 μm and an equal pattern/space. Clear contrast with the $\Delta\phi_{pn}$ image can be obtained by KFM. To further improve the spatial resolution, a smaller probe is required. Mounting a carbon nanotube on the tip of a conventional probe is a promising method.[15,16)]

5. Conclusions

A feedback controller circuit was fabricated to achieve higher response frequency and to improve the spatial resolution. The effect of surface treatment on the contrast of surface potential images was evaluated first. A simple surface treatment method, DHF dipping followed by DI water rinsing, was observed to provide a KFM image with the highest contrast. The XPS analysis indicates that Si–OH bonds replace Si–F bonds after rinsing with DI water so that surface charge is minimized and a high-contrast KFM image can be obtained.

A correlation between surface potential difference and carrier concentration was established. Several methods were employed to determine the surface carrier concentration of a series of samples with different dopant concentrations. They include *C–V* method, SRP, and SIMS. Experimental results confirm a linear correlation between surface carrier concentration and surface potential difference in a log–log plot. According to these correlations, carrier depth profiling by KFM is has been achieved. Peak concentration and junction depth are consistent with the dopant profile determined by SIMS analysis. A high resolution 2-D surface image of a p–n junction array with a pitch as small as 0.8 μm was also demonstrated.

These results indicate that KFM is a very promising technique with which to obtain high resolution 2D carrier profiles of semiconductor devices. Higher resolution could be achieved with a smaller probe tip such as a carbon nanotube.

Acknowledgements

This work was supported by the National Science Council, Taiwan, R.O.C., under contract No. NSC-95-2221-E-009-302-MY3. We also thank the National Nano Device Laboratory, Hsinchu, National Tsing-Hua University, Hsinchu, and Nano Facility Center of National Chiao-Tung University, Hsinchu, Taiwan.

1) M. G. Dowsett and G. A. Cooke: J. Vac. Sci. Technol. B **10** (1992) 353.
2) R. von Criegern, F. Jahnel, M. Bianco, and R. Lange-Gieseler: J. Vac. Sci. Technol. B **12** (1994) 234.
3) G. Binnig, H. Rohrer, Ch. Gerber, and E. Weibel: Phys. Rev. Lett. **49** (1982) 57.
4) G. Binnig, C. F. Quate, and Ch. Gerber: Phys. Rev. Lett. **56** (1986) 930.
5) C. C. Williams, J. Slinkman, W. P. Hough, and H. K. Wickramasinghe: Appl. Phys. Lett. **55** (1989) 1662.
6) G. Neubauer, A. Erickson, C. C. Williams, J. J. Kopanski, M. Rodgers, and D. Adderton: J. Vac. Sci. Technol. B **14** (1996) 426.
7) M. L. O'Malley, G. L. Timp, S. V. Moccio, J. P. Garno, and R. N. Kleiman: Appl. Phys. Lett. **74** (1999) 272.
8) H. Edwards, V. A. Ukraintsev, R. S. Martin, F. S. Johnson, P. Mens, S. Walsh, S. Ashburn, K. S. Wills, K. Harvey, and M. C. Chang: J. Appl. Phys. **87** (2000) 1485.
9) P. A. Rosenthal, Y. Taur, and E. T. Yu: Appl. Phys. Lett. **81** (2002) 3993.
10) H. Edwards, R. McGlothlin, R. S. Martin, E. U. M. Gribelyuk, R. Mahaffy, C. K. Shih, R. S. List, and V. A. Ukraintsev: Appl. Phys. Lett. **72** (1998) 698.
11) M. Nonnenmacher, M. P. O'Boyle, and H. K. Wickramasinghe: Appl. Phys. Lett. **58** (1991) 2921.
12) A. Kikukawa, S. Hosala, and R. Imura: Appl. Phys. Lett. **66** (1995) 3510.
13) G. H. Buh, H. J. Chung, J. H. Yi, I. T. Yoon, and Y. Kuk: J. Appl. Phys. **90** (2001) 443.
14) J. M. R. Weaver and D. W. Abraham: J. Vac. Sci. Technol. B **9** (1991) 1559.
15) S. S. Wong, A. T. Woolley, T. W. Odom, J.-L. Huang, P. Kim, D. V. Vezenov, and C. M. Lieber: Appl. Phys. Lett. **73** (1998) 3465.
16) C. L. Cheung, J. H. Hafner, T. W. Odom, K. Kim, and C. M. Lieber: Appl. Phys. Lett. **76** (2000) 3136.
17) H. Sugimura, Y. Ishia, K. Hayashi, O. Takai, and N. Nakagiri: Appl. Phys. Lett. **80** (2002) 1459.
18) O. Vatel and M. Tanimoto: J. Appl. Phys. **77** (1995) 2358.
19) S. M. Sze: *Physics of Semiconductor Device* (Wiley, New York, 1981) 2nd ed., p. 362.
20) D. K. Schroder: *Semiconductor Material and Device Characterization* (Wiley, New York, 1998) 2nd ed., p. 62.
21) E. F. Schubert, J. M. Kuo, and R. F. Kopf: J. Electron. Mater. **19** (1990) 521.
22) R. G. Wilson, F. A. Stevie, and C. W. Magee: *Secondary Ion Mass Spectrometry—A Practical Handbook for Depth Profiling and Bulk Impurity Analysis* (Wiley, New York, 1989).
23) D. K. Schroder: *Semiconductor Material and Device Characterization* (Wiley, New York, 1998) 2nd ed., p. 31.
24) S. Wolf and R. N. Tauber: *Silicon Processing for the VLSI Era* (Lattice Press, Sunset Beach, CA, 2001), p. 353.
25) T. Takahagi, A. Ishitani, and H. Kuroda: J. Appl. Phys. **69** (1991) 803.
26) D. Graf, M. Grundner, and R. Schulz: J. Appl. Phys. **68** (1990) 5155.
27) C. D. Wagner, W. M. Riggs, L. E. Davis, and J. F. Moulder: *Handbook of X-ray Photoelectron Spectroscopy* (Perkin-Elmer, Waltham, MA, 1979).
28) W. Mönch: *Semiconductor Surface and Interface* (Springer, Heidelberg, 1995) 2nd ed., p. 54.